Multioctave supercontinuum from visible to mid-infrared and bend effects on ultrafast nonlinear dynamics in gas-filled hollow-core fiber

Habib, Md Selim; Markos, Christos; Antonio-Lopez, J. E.; Amezcua-Correa, Rodrigo

Published in:
Applied Optics

Link to article, DOI:
10.1364/AO.58.0000D7

Publication date:
2019

Document Version
Publisher's PDF, also known as Version of record

Research Article Vol. 58, No. 13 / 1 May 2019 / Applied Optics D7

applied optics

Multioctave supercontinuum from visible to mid-infrared and bend effects on ultrafast nonlinear dynamics in gas-filled hollow-core fiber

Md Selim Habib,[1,*] Christos Markos,[2] J. E. Antonio-Lopez,[1] and Rodrigo Amezcua-Correa[1]

[1]CREOL, The College of Optics and Photonics, University of Central Florida, Florida 32816, USA
[2]DTU Fotonik, Technical University of Denmark, DK-2800, Denmark
*Corresponding author: mdselim.habib@creol.ucf.edu

Received 26 November 2018; revised 23 January 2019; accepted 26 January 2019; posted 28 January 2019 (Doc. ID 351456); published 6 March 2019

Broadband supercontinuum generation is numerically investigated in a Xe-filled nested hollow-core antiresonant (HC-AR) fiber pumped at 3 μm with pulses of 100 fs duration and 15 μJ energy. For a 25 cm long fiber, under 7 bar pressure, the supercontinuum spectrum spans multiple octaves from 400 nm to 5000 nm. Furthermore, the influence of bending on ultrafast nonlinear pulse propagation dynamics is investigated for two types of HC-AR fibers (nested and non-nested capillaries). Our results predict similar nonlinear dynamics for both fiber types and a significant reduction of the spectral broadening under tight bending conditions.

https://doi.org/10.1364/AO.58.0000D7

1. INTRODUCTION

Hollow-core antiresonant (HC-AR) fibers are a versatile platform for investigating ultrafast nonlinear optics in gas-filled fibers because of their broadband guidance, low loss (near-IR to mid-IR), high damage threshold, and weak and anomalous dispersion [1–10]. The possibility of filling these fibers with gases bestows them with a nonlinearity and dispersion that can be adjusted with pressure [8,11]. Moreover, gases have several distinct advantages over solid nonlinear materials such as higher damage thresholds, and extremely wide transparency ranges, and they are also considered a self-healing media due to their ability to recombine after ionization [8,12–15]. In previous works, light–gas interaction and soliton dynamics in noble gas-filled HC fibers of Kagome type (also known as inhibited-coupling fibers) have been extensively studied in the near-IR [8,10,11,13,14]. The prospect for further increasing the bandwidth by fiber tapering was first demonstrated for HC fibers in [16]. However, limited studies on light–gas interaction have been performed in the mid-IR spectral regime [12,17–19]. The mid-IR region is attractive mainly because most molecules display their fundamental vibrational absorptions in this wavelength range [20,21]. Therefore, mid-IR supercontinuum sources are currently of great technical and scientific interest due to their wide range of potential applications such as early cancer diagnostics [22], food quality control [23], medical surgery [24], and thermal and photoacoustic imaging [25,26] or spectroscopy [27]. The supercontinuum sources, both in the visible, near-IR, and mid-IR, have so high brightness that they outperform square km-sized synchrotrons, as demonstrated recently [28]. Moreover, near-IR to mid-IR supercontinuum sources find applications in the extremely important imaging modalities of hyperspectral imaging [29,30], photoacoustic sensing of glucose [31], and optical coherence tomography imaging [32,33], as well as in disease detection [22].

One of the most challenging aspects of generating supercontinuum in the mid-IR using silica-based fibers is that silica glass has a high attenuation beyond 3 μm [34]. Nonetheless, the high attenuation of silica in the mid-IR was overcome with the development of HC fibers, which enabled high light confinement in the core (~99.99%) and therefore loss levels in the order of dB/m [2,24,35]. These efforts lead to the demonstration of minimum propagation loss of 34 dB/km at 3050 nm [2] and light guidance beyond 5 μm [36].

Despite their unique optical properties, HC-AR fibers have been found to be sensitive to bend perturbations. The best bend performance of HC-AR fibers has been recently experimentally demonstrated in the mid-IR with a loss of 0.3 dB/m at a 8 cm bend radius [37]. However, to the best of our knowledge, the effect of bending on ultrafast nonlinear propagation dynamics has never been investigated, and it still remains unknown.

In this work, we start our investigation with the main supercontinuum generation dynamics in gas-filled HC-AR fibers pumped in the mid-IR. We show multiple octave-spanning supercontinua covering the 400–5000 nm spectral range using a 25 cm nested HC-AR fiber. It should be noted that our

numerical simulations consider experimental feasible parameters, i.e., 100 fs pulse duration and 15 μJ pulse energy at 3 μm (Spitfire Pro, Spectra Physics). Towards the development of compact mid-IR supercontinuum sources, coiling of fiber with relatively small bending radius is perhaps a crucial step [37–39]. In Ref. [38], it has been shown experimentally that it is possible to coil HC-AR fiber tightly (bend radius <5 cm) with minimum loss of 0.2 dB/m. In addition, bending of the fiber is a well-known experimental method to suppress the higher order modes, making the fiber effectively single-mode [38]. We consider two different HC-AR fibers with the same core diameter but one with nested HC-AR fiber (smaller capillaries are nested inside the tubes defining the core boundary) and a second fiber without nested capillaries. This way, we can determine whether a nested fiber structure (which imposes fabrication challenges) could have a direct impact on the performance. Our numerical results predict that the blue edge of the supercontinuum is affected at a critical bend radius of ~12 cm, whereas both the short and long wavelength edge of the supercontinuum are strongly affected for a bend radius smaller than 5 cm. Our investigations also indicate that the nested HC-AR fiber and the non-nested HC-AR fiber show similar nonlinear propagation dynamics when a short section of fiber (25 cm) is considered, although the former has lower loss than the latter.

2. FIBER GEOMETRY AND MODELING

In order to determine realistic loss and dispersion of the nested HC-AR fiber, which was fabricated in house, we retrieved its exact geometry from a scanning electron microscope (SEM) image [inset of Fig. 1(a)] [40]. The fiber was specifically designed to guide light up to 6 μm with core/outer capillary/inner capillary diameters of 97/66/19 μm and average wall thicknesses of the inner and outer tubes of 2000 ± 50 nm and 1000 ± 50 nm. The outer tube wall thickness was chosen such as to guarantee low loss at the pump wavelength of 3.0 μm. Moreover, the first high-loss resonance band located at around 2.1 μm is far away from the pump wavelength. Figures 1(a) and 1(b) show the effective refractive index and loss of the fundamental LP_{01} core mode for the evacuated HC-AR fiber and the loss, both calculated using finite element modeling (FEM). To accurately predict the leakage loss and surface scattering loss (SSL) [6], we employed a perfectly matched layer outside the fiber structure. Both the mesh size and perfectly matched layer parameters were carefully optimized according to [3,6]. The fraction of power in silica was found so to estimate the effective material loss and added to the leakage loss and SSL in order to obtain the total propagation loss. Attenuation data for the fused silica glass was obtained from Humbach *et al.* [34]. The fiber exhibits broadband guidance from the near-IR to the mid-IR spectral range with low propagation loss [Fig. 1(b), red solid line] despite the high attenuation of silica glass beyond 3 μm. This is due to the fact that there is low overlap between the fundamental guiding mode and the silica struts (dashed gray line).

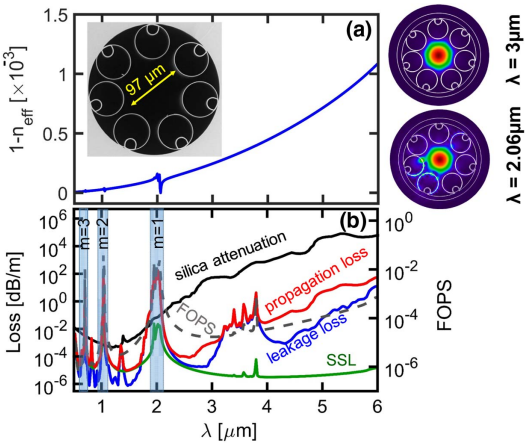

Fig. 1. Calculated (a) effective refractive index (n_{eff}) of LP_{01}-like mode and (b) loss (left) and fraction of power in silica (right) of an evacuated nested HC-AR fiber. The fiber has a core diameter ~97 μm, an average larger and smaller capillary diameter 66 μm and 19 μm, respectively, and average wall thickness of the inner and outer tubes is 2000 ± 50 nm and 1000 ± 50 nm, respectively. The light blue bars in (b) show the resonance bands, with $m = 1, 2, 3$. Inset of (a), scanning electron microscope image of fabricated nested HC-AR fiber. Right-hand side of (a), mode field profile at 3 μm (pump wavelength) and 2.06 μm (on-resonance). FOPS, fraction of power in silica.

3. MODELING OF PULSE PROPAGATION

The optical pulse propagation in the gas-filled HC-AR fiber was numerically calculated using a unidirectional pulse propagation equation considering single polarization [12,13],

$$\partial_z E(z,\omega) = i\left(\beta(\omega) - \frac{\omega}{v_g} + i\frac{\alpha}{2}\right)E(z,\omega) + i\frac{\omega^2}{2c^2\beta(\omega)}F(\chi^{(3)}E^3), \quad (1)$$

where z is the propagation direction, t is the time in the reference frame moving with the pump group velocity v_g, $E(z,\omega)$ is the electric field in the frequency domain, ω is the angular frequency, $\alpha(\omega)$ is the propagation loss, c is the vacuum speed of light, $\beta(\omega)$ is the propagation constant, F denotes the Fourier transform, and $\chi^{(3)}$ is the third-order nonlinear susceptibility. The nonlinear refractive index (n_2) of Xe at 7 bar was set to 4.76×10^{-22} m^2/W and assumed to be wavelength independent [12,41]. Due to the very low light–glass overlap (≪1%) and a peak intensity too low to ionize the gas and form a plasma (30 TW/cm^2, free electron generation of ~6×10^{19} m^{-3}), we neglected the Raman contribution and nonlinear polarization due to photoionization, respectively.

4. RESULTS AND DISCUSSION

A. Ultrafast Nonlinear Dynamics in Straight Fiber

The spectral and temporal evolution in a 25 cm long Xe-filled nested HC-AR fiber under 7 bar pressure and pumped at 3.0 μm (in the anomalous dispersion regime) with a 100 fs Gaussian pulse and pulse energy of 15 μJ corresponds to soliton order of ~7.3, and they are shown in Figs. 2(c) and 2(e), respectively. Due to the interplay between self-phase modulation (SPM) and anomalous dispersion, the pulse experiences strong soliton self-compression down to ~3 fs (less than a single cycle) with peak intensity ~30 TW/cm^2 after propagating 14 cm, as shown in Fig. 2(d). At this point, a dispersive wave (DW) is

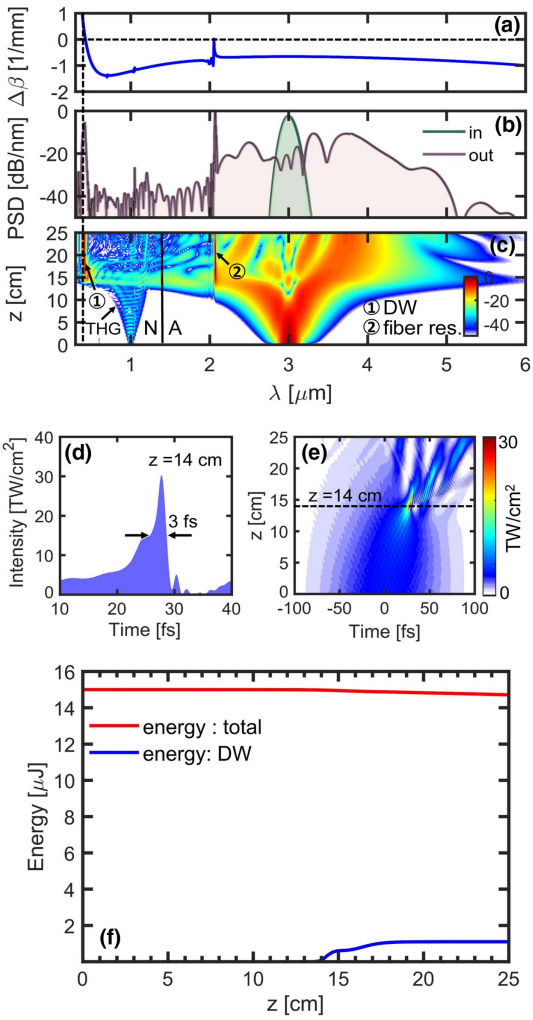

Fig. 2. Calculated (a) propagation constant mismatch between solitons and dispersive waves, (b) power spectral density (PSD) at $z = 0$ and $z = 25$ cm, (c) spectral evolution, (d) intensity at the maximum compression point at $z = 14$ cm, (e) temporal evolution, and (f) total energy (blue) and energy of dispersive wave (red) as a function of fiber length for a ~97 μm core nested HC-AR fiber under 7 bar Xe, pulse energy 15 μJ, and pulse duration 100 fs pumping in the anomalous dispersion regime at 3 μm. *N*, normal dispersion regime; *A*, anomalous dispersion regime; THG, third-harmonic generation; DW, dispersive wave. The dashed vertical line in (a–c) indicates DW emission at 415 nm.

emitted at 415 nm. The DW emission at 415 nm is also confirmed by calculating the propagation constant mismatch $\Delta\beta$, between the soliton and DWs, which is shown in Fig. 2(a). The $\Delta\beta$ was calculated using the following expression [14]:

$$\Delta\beta(\omega) \approx \beta(\omega) - (\beta_0 + (\omega - \omega_0)\beta_1 + \gamma N P_0 \omega/\omega_0), \quad (2)$$

where β_0 is the propagation constant, $\beta_1 = 1/v_g$ is the inverse group velocity at ω_0, P_0 is the pump peak power, N is the soliton order, $\gamma = n_2/cA_{\text{eff}}$ is the fiber nonlinear coefficient, and A_{eff} is the effective mode area of the fiber.

A multiple-octave-spanning supercontinuum from ~400 nm to ~5000 nm is obtained after propagating 25 cm, as shown in Fig. 2(b). The power spectral density was calculated as [42]

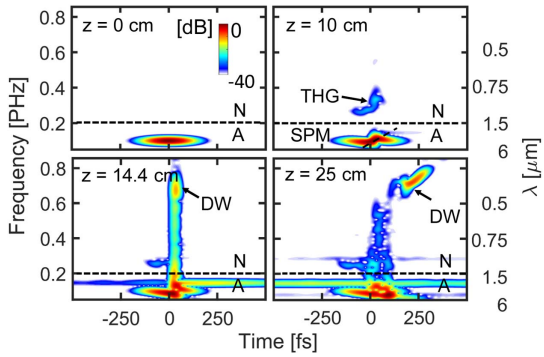

Fig. 3. Spectrogram at selected distances of the simulation depicted in Fig. 2. The spectrogram was calculated using a 25 fs Gaussian gate pulse. THG, third-harmonic generation.

$\text{PSD} = \frac{c}{\lambda^2}|E(z,\lambda)|^2 f_{\text{rep}}$, where f_{rep} is the seed laser repetition rate. A narrowband emission peak is observed at the resonance wavelength at ~2.1 μm despite of the high loss at this wavelength. This narrowband emission feature in the vicinity of the anticrossing is due to the combination of four-wave mixing and the DW emission, recently reported in Refs. [43,44]. Figure 2(f) shows the total energy (blue line) and energy of DW (red line) as a function of propagation distance. It can be seen that the total energy remains almost constant during propagation (total output energy ~14.7 μJ), with a DW formation of ~7.3% efficiency.

Spectrograms at fiber lengths 0 cm, 10 cm, 14 cm, and 20 cm show the nonlinear dynamics (Fig. 3). At $z = 10$ cm, SPM takes place, which causes a temporal pulse compression and a positive nonlinear chirp across the pulse, indicated by the dashed line through pulse center. At $z = 14$ cm, the pulse is highly compressed to ~3 fs and maximally spectrally broadened due to the soliton self-compression effect, reaching a peak intensity of ~30 TW/cm^2. Additionally, a DW is emitted in the normal dispersion regime at 415 nm, and self-steepening causes an asymmetry in the pulse. During further propagation, DW widens linearly in the time domain, which is clearly seen from the spectrogram snapshot at $z = 25$ cm.

B. Ultrafast Nonlinear Dynamics in Bend Fibers

In this section, we investigate and discuss the effects of bending on the HC-AR fibers and the generated supercontinuum. Figure 4 shows the bend loss as a function of bend radius at 3 μm for two different fibers: nested (red line) and non-nested (blue line). The bend loss was calculated using [6] $n_b = n(x,y)e_b^{(x/R)}$, where R_b is the bend radius, x is the direction of bend, $n(x,y)$ is the refractive index profile of the straight fiber, and n_b is the equivalent refractive index after bending. As expected, the nested fiber has a lower loss compared to the non-nested fiber owing to the fact that nested tubes increase the inhibited coupling between the fundamental core mode and the cladding modes, and thereby reducing the loss [3,6,7]. The non-nested HC-AR fiber shows two high-loss peaks at two different bend radii of 11 cm and 19 cm, whereas only one low-loss peak with relatively low loss at 8.5 cm is found for the nested HC-AR fiber. The loss peaks are observed mainly due to the coupling between the core modes and the cladding

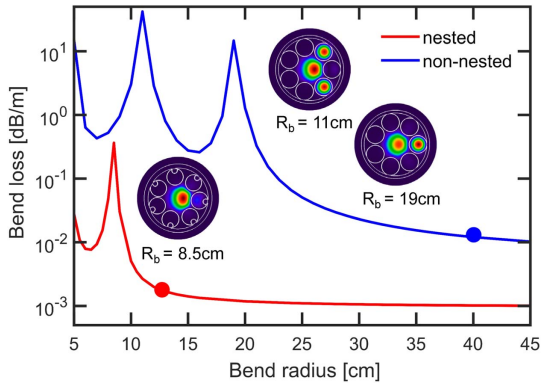

Fig. 4. Total bend loss as a function of bend radius at 3 μm. The solid red and blue dot markers indicate critical bend radius.

(tubes) modes [3,6], which can be also seen from the mode field profiles at $R_b = 11$ cm, 19 cm (non-nested HC-AR fiber), and 8.5 cm (nested HC-AR fiber) in Fig. 4. The critical bend radius R_{cr} is indicated by the solid dot markers in Fig. 4, and the critical bend radius is defined to be where the straight propagation loss is doubled [6]. Moreover, the non-nested fiber has significantly larger critical bend radius ($R_{cr} = 40$ cm) than the nested HC-AR fiber ($R_{cr} = 12$ cm). Despite its large core diameter, the bend loss profile indicates that the nested HC-AR fiber can be coiled to a reasonably small bend radius. Subsequently, we investigated the impact of moderate and small bending radii on the overall loss and supercontinuum generation (see Fig. 5).

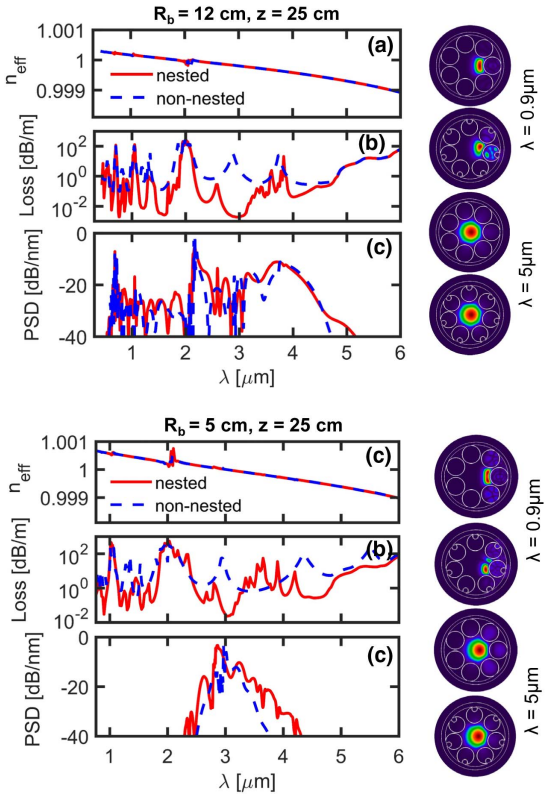

Fig. 5. Calculated (a) effective refractive index (n_{eff}) of LP_{01}-like mode, (b) propagation loss (left), and (c) PSD at $z = 25$ cm under the bend radius $R_b = 12$ cm (top) and $R_b = 5$ cm (bottom). Right-hand side of both figures shows mode field profile for nested and non-nested HC-AR fiber at 0.9 μm and 5 μm.

1. Moderate Bend Radius

First, we consider the case when both nested and non-nested fibers are coiled with a bend radius of $R_b = 12$ cm (R_{cr} for nested HC-AR fiber). Figure 5(b) (top) indicates that the nested HC-AR fiber has better loss performance than the non-nested HC-AR fiber, up to 4.8 μm, while beyond 4.8 μm, both fibers exhibit almost equal loss values and spectra. When the fibers are bent to 12 cm, the blue (short) edge of the supercontinuum shifts towards longer wavelengths, 700 nm as opposed to 400 nm for straight fibers, [see Fig. 2(b)], whereas the red (long) edge of the supercontinuum remains almost unaffected.

2. Small Bend Radius

Next, a smaller bend radius of 5 cm was considered. The smaller coil radius leads to a significant reduction of the spectral broadening as displayed in Fig. 5 (bottom). The reduction in the supercontinuum is owing to the fact that the dispersion is highly influenced under a small bend radius, and essentially no soliton can be formed. In this case, the spectral broadening is mainly due to the SPM unlike for the straight fiber and larger bend radius cases.

5. CONCLUSION

In conclusion, we numerically demonstrated multiple-octave-spanning supercontinuum generation covering 400–5000 nm based on a Xe-filled HC-AR fiber, considering experimentally feasible fiber and laser parameters. For the first time, to the best of our knowledge, nonlinear pulse propagation dynamics were investigated under different bend conditions, and we show that supercontinuum generation is strongly influenced by a small bend radius. Despite the better overall loss performance of nested fibers, comparable spectra are obtained for both fiber types. This indicates that for this particular nonlinear application, complex nested fibers (in terms of fiber fabrication) can be avoided. As practical implementation of gas-filled HC fiber sources could require compact fiber coiling, understanding the impact of fiber design and bending on ultrafast nonlinear dynamics will be beneficial for bend-sensitive applications.

Funding. Army Research Office (ARO) (W911NF-12-1-0450, W911NF-17-1-0501); Air Force Office of Scientific Research (AFOSR) (FA9550-15-10041); Det Frie Forskningsråd (DFF) (4184-00359B, 8022-00091A).

REFERENCES

1. A. D. Pryamikov, A. S. Biriukov, A. F. Kosolapov, V. G. Plotnichenko, S. L. Semjonov, and E. M. Dianov, "Demonstration of a waveguide regime for a silica hollow—core microstructured optical fiber with a negative curvature of the core boundary in the spectral region > 3.5 μm," Opt. Express **19**, 1441–1448 (2011).
2. F. Yu, W. J. Wadsworth, and J. C. Knight, "Low loss silica hollow core fibers for 3–4 μm spectral region," Opt. Express **20**, 11153–11158 (2012).
3. M. S. Habib, O. Bang, and M. Bache, "Low-loss hollow-core silica fibers with adjacent nested anti-resonant tubes," Opt. Express **23**, 17394–17406 (2015).

4. M. S. Habib, O. Bang, and M. Bache, "Low-loss single-mode hollow-core fiber with anisotropic anti-resonant elements," Opt. Express **24**, 8429–8436 (2016).
5. M. S. Habib, O. Bang, and M. Bache, "Low-loss hollow-core anti-resonant fibers with semi-circular nested tubes," IEEE J. Sel. Top. Quantum Electron. **22**, 156–161 (2016).
6. F. Poletti, "Nested antiresonant nodeless hollow core fiber," Opt. Express **22**, 23807–23828 (2014).
7. W. Belardi and J. C. Knight, "Hollow antiresonant fibers with reduced attenuation," Opt. Lett. **39**, 1853–1856 (2014).
8. P. S. J. Russell, P. Hölzer, W. Chang, A. Abdolvand, and J. C. Travers, "Hollow-core photonic crystal fibres for gas-based nonlinear optics," Nat. Photonics **8**, 278–286 (2014).
9. F. Couny, F. Benabid, P. J. Roberts, P. S. Light, and M. G. Raymer, "Generation and photonic guidance of multi-octave optical-frequency combs," Science **318**, 1118–1121 (2007).
10. T. Balciunas, C. Fourcade-Dutin, G. Fan, T. Witting, A. A. Voronin, A. M. Zheltikov, F. Gerome, G. G. Paulus, A. Baltuska, and F. Benabid, "A strong-field driver in the single-cycle regime based on self-compression in a kagome fibre," Nat. Commun. **6**, 6117 (2015).
11. M. F. Saleh, W. Chang, P. Hölzer, A. Nazarkin, J. C. Travers, N. Y. Joly, P. S. J. Russell, and F. Biancalana, "Theory of photoionization-induced blueshift of ultrashort solitons in gas-filled hollow-core photonic crystal fibers," Phys. Rev. Lett. **107**, 203902 (2011).
12. M. S. Habib, C. Markos, O. Bang, and M. Bache, "Soliton-plasma nonlinear dynamics in mid-IR gas-filled hollow-core fibers," Opt. Lett. **42**, 2232–2235 (2017).
13. W. Chang, A. Nazarkin, J. C. Travers, J. Nold, P. Hölzer, N. Y. Joly, and P. S. J. Russell, "Influence of ionization on ultrafast gas-based nonlinear fiber optics," Opt. Express **19**, 21018–21027 (2011).
14. J. C. Travers, W. Chang, J. Nold, N. Y. Joly, and P. S. J. Russell, "Ultrafast nonlinear optics in gas-filled hollow-core photonic crystal fibers [Invited]," J. Opt. Soc. Am. B **28**, A11–A26 (2011).
15. C. Markos, J. C. Travers, A. Abdolvand, B. J. Eggleton, and O. Bang, "Hybrid photonic-crystal fiber," Rev. Mod. Phys. **89**, 045003 (2017).
16. M. S. Habib, C. Markos, J. E. Antonio-Lopez, R. A. Correa, O. Bang, and M. Bache, "Multi-stage generation of extreme ultraviolet dispersive waves by tapering gas-filled hollow-core anti-resonant fibers," Opt. Express **26**, 24357–24371 (2018).
17. M. Gebhardt, C. Gaida, T. Heuermann, F. Stutzki, C. Jauregui, J. Antonio-Lopez, A. Schulzgen, R. Amezcua-Correa, J. Limpert, and A. Tünnermann, "Nonlinear pulse compression to 43 W GW-class few-cycle pulses at 2 μm wavelength," Opt. Lett. **42**, 4179–4182 (2017).
18. A. I. Adamu, M. S. Habib, C. R. Petersen, B. Zhou, A. Schülzgen, J. E. Antonio-Lopez, R. Amezcua-Correa, O. Bang, and C. Markos, "Supercontinuum generation from deep-UV to mid-IR in a noble gas-filled fiber pumped with ultrashort mid-IR pulses," in *Advanced Photonics 2018 (BGPP, IPR, NP, NOMA, Sensors, Networks, SPPCom, SOF)* (Optical Society of America, 2018), paper JTu6E.2.
19. A. I. Adamu, M. S. Habib, C. R. Petersen, J. E. Antonio-Lopez, B. Zhou, A. Schülzgen, R. Amezcua-Correa, O. Bang, and C. Markos, "Deep-UV to mid-IR supercontinuum generation driven by mid-IR ultrashort pulses in a gas-filled fiber," arXiv:1805.03118 [physics] (2018).
20. A. Schliesser, N. Picqué, and T. W. Hänsch, "Mid-infrared frequency combs," Nat. Photonics **6**, 440–449 (2012).
21. C. R. Petersen, U. Møller, I. Kubat, B. Zhou, S. Dupont, J. Ramsay, T. Benson, S. Sujecki, N. Abdel-Moneim, Z. Tang, D. Furniss, A. Seddon, and O. Bang, "Mid-infrared supercontinuum covering the 1.4–13.3 μm molecular fingerprint region using ultra-high NA chalcogenide step-index fibre," Nat. Photonics **8**, 830–834 (2014).
22. A. B. Seddon, "A prospective for new mid-infrared medical endoscopy using chalcogenide glasses," Int. J. Appl. Glass Sci. **2**, 177–191 (2011).
23. J. W. M. Wegener, W. P. Cofino, E. A. Maier, and G. N. Kramer, "The preparation, testing and certification of two freshwater sediment reference materials for polycyclic aromatic hydrocarbons and polychlorinated biphenyls: BCR CRM 535 and CRM 536," TrAC Trends Anal. Chem. **18**, 14–25 (1999).
24. A. Urich, R. R. J. Maier, F. Yu, J. C. Knight, D. P. Hand, and J. D. Shephard, "Flexible delivery of Er:YAG radiation at 2.94 μm with negative curvature silica glass fibers: a new solution for minimally invasive surgical procedures," Biomed. Opt. Express **4**, 193–205 (2013).
25. Y. Matsuura and K. Naito, "Flexible hollow optical fiber bundle for infrared thermal imaging," Biomed. Opt. Express **2**, 65–70 (2011).
26. M. K. Dasa, C. Markos, M. Maria, C. R. Petersen, P. M. Moselund, and O. Bang, "High-pulse energy supercontinuum laser for high-resolution spectroscopic photoacoustic imaging of lipids in the 1650–1850 nm region," Biomed. Opt. Express **9**, 1762 (2018).
27. C. R. Petersen, R. D. Engelsholm, C. Markos, L. Brilland, C. Caillaud, J. Trolès, and O. Bang, "Increased mid-infrared supercontinuum bandwidth and average power by tapering large-mode-area chalcogenide photonic crystal fibers," Opt. Express **25**, 15336–15348 (2017).
28. C. R. Petersen, P. M. Moselund, L. Huot, L. Hooper, and O. Bang, "Towards a table-top synchrotron based on supercontinuum generation," Infrared Phys. Technol. **91**, 182–186 (2018).
29. C. R. Petersen, N. Prtljaga, M. Farries, J. Ward, B. Napier, G. R. Lloyd, J. Nallala, N. Stone, and O. Bang, "Mid-infrared multispectral tissue imaging using a chalcogenide fiber supercontinuum source," Opt. Lett. **43**, 999–1002 (2018).
30. S. Dupont, C. Petersen, J. Thøgersen, C. Agger, O. Bang, and S. R. Keiding, "IR microscopy utilizing intense supercontinuum light source," Opt. Express **20**, 4887–4892 (2012).
31. M. K. Dasa, C. Markos, J. Janting, and O. Bang, "Multispectral photoacoustic sensing for accurate glucose monitoring using a supercontinuum laser," J. Opt. Soc. Am. B **36**, A61–A65 (2019).
32. N. M. Israelsen, C. R. Petersen, A. Barh, D. Jain, M. Jensen, G. Hannesschläger, P. Tidemand-Lichtenberg, C. Pedersen, A. Podoleanu, and O. Bang, "Real-time high-resolution mid-infrared optical coherence tomography," arXiv:1810.05445 [physics] (2018).
33. N. M. Israelsen, M. Maria, M. Mogensen, S. Bojesen, M. Jensen, M. Haedersdal, A. Podoleanu, and O. Bang, "The value of ultrahigh resolution OCT in dermatology—delineating the dermo-epidermal junction, capillaries in the dermal papillae and vellus hairs," Biomed. Opt. Express **9**, 2240–2265 (2018).
34. O. Humbach, H. Fabian, U. Grzesik, U. Haken, and W. Heitmann, "Analysis of OH absorption bands in synthetic silica," J. Non-Cryst. Solids **203**, 19–26 (1996).
35. M. Michieletto, J. K. Lyngsø, C. Jakobsen, J. Lægsgaard, O. Bang, and T. T. Alkeskjold, "Hollow-core fibers for high power pulse delivery," Opt. Express **24**, 7103–7119 (2016).
36. A. N. Kolyadin, A. F. Kosolapov, A. D. Pryamikov, A. S. Biriukov, V. G. Plotnichenko, and E. M. Dianov, "Light transmission in negative curvature hollow core fiber in extremely high material loss region," Opt. Express **21**, 9514–9519 (2013).
37. W. Belardi and J. C. Knight, "Hollow antiresonant fibers with low bending loss," Opt. Express **22**, 10091–10096 (2014).
38. S.-F. Gao, Y.-Y. Wang, X.-L. Liu, W. Ding, and P. Wang, "Bending loss characterization in nodeless hollow-core anti-resonant fiber," Opt. Express **24**, 14801–14811 (2016).
39. R. M. Carter, F. Yu, W. J. Wadsworth, J. D. Shephard, T. Birks, J. C. Knight, and D. P. Hand, "Measurement of resonant bend loss in anti-resonant hollow core optical fiber," Opt. Express **25**, 20612–20621 (2017).
40. J. R. Hayes, S. R. Sandoghchi, T. D. Bradley, Z. Liu, R. Slavík, M. A. Gouveia, N. V. Wheeler, G. Jasion, Y. Chen, E. N. Fokoua, M. N. Petrovich, D. J. Richardson, and F. Poletti, "Antiresonant hollow core fiber with an octave spanning bandwidth for short haul data communications," J. Lightwave Technol. **35**, 437–442 (2017).
41. S. Zahedpour, J. K. Wahlstrand, and H. M. Milchberg, "Measurement of the nonlinear refractive index of air constituents at mid-infrared wavelengths," Opt. Lett. **40**, 5794–5797 (2015).
42. C. Agger, C. Petersen, S. Dupont, H. Steffensen, J. K. Lyngsø, C. L. Thomsen, J. Thøgersen, S. R. Keiding, and O. Bang, "Supercontinuum generation in ZBLAN fibers—detailed comparison between measurement and simulation," J. Opt. Soc. Am. B **29**, 635–645 (2012).
43. F. Tani, F. Köttig, D. Novoa, R. Keding, and P. S. J. Russell, "Effect of anti-crossings with cladding resonances on ultrafast nonlinear dynamics in gas-filled photonic crystal fibers," Photon. Res. **6**, 84–88 (2018).
44. F. Meng, B. Liu, S. Wang, J. Liu, Y. Li, C. Wang, A. M. Zheltikov, and M. Hu, "Controllable two-color dispersive wave generation in argon-filled hypocycloid-core kagome fiber," Opt. Express **25**, 32972–32984 (2017).